

P. Jacquet, L. Colas, M.-L. Mayoral, G. Arnoux, V. Bobkov, M. Brix, P. Coad,
A. Czarnecka, D. Dodt, F. Durodie, A. Ekedahl, D. Frigione, M. Fursdon,
E. Gauthier, M. Goniche, M. Graham, E. Joffrin, A. Korotkov, E. Lerche,
J. Mailloux, I. Monakhov, C. Noble, J. Ongena, V. Petrzilka, C. Portafaix,
F. Rimini, A. Sirinelli, V. Riccardo, Z. Vizvary, A. Widdowson,
K.-D. Zastrow and JET EFDA contributors

Heat-Loads on JET Plasma Facing Components from ICRF and LH Wave Absorption in the SOL

“This document is intended for publication in the open literature. It is made available on the understanding that it may not be further circulated and extracts or references may not be published prior to publication of the original when applicable, or without the consent of the Publications Officer, EFDA, Culham Science Centre, Abingdon, Oxon, OX14 3DB, UK.”

“Enquiries about Copyright and reproduction should be addressed to the Publications Officer, EFDA, Culham Science Centre, Abingdon, Oxon, OX14 3DB, UK.”

The contents of this preprint and all other JET EFDA Preprints and Conference Papers are available to view online free at www.iop.org/Jet. This site has full search facilities and e-mail alert options. The diagrams contained within the PDFs on this site are hyperlinked from the year 1996 onwards.

Heat-Loads on JET Plasma Facing Components from ICRF and LH Wave Absorption in the SOL

P. Jacquet¹, L. Colas², M.-L. Mayoral¹, G. Arnoux¹, V. Bobkov³, M. Brix¹, P. Coad¹, A. Czarnecka⁴, D. Dodt³, F. Durodie⁵, A. Ekedahl², D. Frigione⁶, M. Fursdon¹, E. Gauthier², M. Goniche², M. Graham¹, E. Joffrin², A. Korotkov¹, E. Lerche⁵, J. Mailloux¹, I. Monakhov¹, C. Noble¹, J. Ongena⁵, V. Petrzilka⁷, C. Portafaix², F. Rimini⁸, A. Sirinelli¹, V. Riccardo¹, Z. Vizvary¹, A. Widdowson², K.-D. Zastrow¹ and JET EFDA contributors*

JET-EFDA, Culham Science Centre, OX14 3DB, Abingdon, UK

¹*EURATOM-CCFE Fusion Association, Culham Science Centre, OX14 3DB, Abingdon, OXON, UK*

²*CEA, IRFM, F-13108 Saint-Paul-Lez-Durance*

³*Max-Planck-Institut für Plasmaphysik, EURATOM-Assoziation, Garching, Germany*

⁴*Association Euratom-IPPLM, Hery 23, 01-497 Warsaw, Poland*

⁵*Association EURATOM-Belgian State, ERM-KMS, Brussels, Belgium*

⁶*EURATOM-ENEA sulla Fusione, C.R. Frascati, Roma, Italy*

⁷*Association EURATOM-IPP.CR, Za Slovankou 3, 182 21 Praha 8, Czech Republic*

⁸*EFDA-CSU, Culham Science Centre, OX14 3DB, Abingdon, OXON, UK*

* See annex of F. Romanelli et al, "Overview of JET Results", (23rd IAEA Fusion Energy Conference, Daejeon, Republic of Korea (2010)).

ABSTRACT.

In JET, Lower Hybrid (LH) and Ion Cyclotron Resonance Frequency (ICRF) wave absorption in the Scrape-Off Layer (SOL) can lead to enhanced heat fluxes on some Plasma Facing Components (PFCs). Experiments have been carried out to characterize these heat loads in order to: (i) prepare JET operation with the Be wall which has a reduced power handling capability as compared to the carbon wall and (ii) better understand the physics driving these wave absorption phenomena and propose solutions for next generation systems to reduce them. When using ICRF, hot spots are observed on the antenna structures and on limiters close to the powered antennae and are explained by acceleration of ions in RF-rectified sheath potentials. High temperatures up to 800°C can be reached on locations where a deposit has built up on tile surfaces. Modelling taking into account the fast thermal response of surface layers can well reproduce surface temperature measurements via IR imaging, and allow evaluation of the heat fluxes local to active ICRF antennae. The flux scales linearly with the SOL density and with the antenna voltage. Strap phasing corresponding to wave spectra with lower k_{\parallel} values can lead to a significant increase of hot spot intensity in agreement with antenna modeling that predicts, in that case, an increase of RF sheath rectification. LH absorption in front of the antenna through Electron Landau Damping of the wave with high N_{\parallel} components generates hot spots precisely located on PFCs magnetically connected to the launcher. Analysis of LH hot spot surface temperature from IR measurements allows quantification of the power flux along the field lines: in worst case scenarios it is in the range of 15-30MW/m². The main driving parameter is the LH power density along the horizontal rows of the launcher, the heat fluxes scaling roughly with the square of LH power density. The local electron density in front of the grill increases with the LH launched power; this also enhances the intensity of the LH hot spots.

1. INTRODUCTION

Ion Cyclotron Resonance Frequency (ICRF) and Lower Hybrid (LH) systems are used in most of the JET scenario development experiments, to provide heating and current drive and also for impurity and MHD control. The addition of ELM resilient matching systems on the JET ICRF antennas has greatly improved the ICRF power availability to H-mode plasmas [1]. For the JET LH system, operation at launched power density close to the ITER target (25MW/m²) was recently confirmed [2]. However, parasitic LH and ICRF wave absorption in the plasma Scrape-Off Layer (SOL) can lead, for the ICRF case, to enhanced impurity release [3] and to enhanced heat fluxes on some Plasma Facing Components (PFCs) [4] [5]. Relatively modest parallel power densities can be an issue in the far SOL because the field lines may not be at grazing incidence on targets. These heat loads, were not an operational issue with the carbon wall, but from 2011, JET will operate with a new ITER-Like wall consisting mainly of Beryllium (Be) tiles in the chamber and tungsten tiles in the divertor [6]. The same choice of material was also made for the ITER first wall. As the heat fluxes tolerated for Be tiles before melting are much lower than for Carbon Fibre reinforced Carbon (CFC) tiles, experiments were carried-out in 2008-2009 to better characterise these wave absorption

phenomena, and determine their driving parameters. This work relied on measurements from an Infra- Red (IR) camera [7] viewing three ICRF antennas, and some PFCs magnetically connected to the LH launcher. In this paper, we present the analysis of surface temperature measurements to quantify heatfluxes corresponding to ICRF and LH power absorption in the JET SOL. Thermal models of some PFCs were specifically developed and as far as possible validated for this purpose. The wide angle IR camera diagnostic is briefly described in section 2 along with a short description of the ICRF and LH antenna systems on JET. The IR measurements deconvolution method used to evaluate heat-fluxes from the time evolution of surface temperature measurements adapted from reference [8] is presented in section 3. Estimation of heat-fluxes implies knowledge of the thermal response of the components studied, which in our case was obtained from modelling. In section 4, we present thermal modelling of JET ICRF antenna A2 septa and evaluation of heat loads from the local effect of RF sheath rectification. The heat flux dependence with RF system parameters and plasma properties are discussed in section 5. Thermal modelling of hot spots from fast electrons accelerated by the electric field in front of the LH launcher, and impinging on poloidal limiters or on the upper dump plates is presented in section 6, and power flux dependence with LH system parameters and SOL plasma properties are described in section 7. Finally the implications of this analysis using measurements with the JET carbon wall are discussed in the context of the future operation with the ITER-Like wall.

2. JET ICRF AND LH SYSTEMS, AND WIDE ANGLE INFRA-RED CAMERA

Figure 1 shows a schematic top view of the JET. The A2 ICRF antennae A, B, C, and D and the ITER-Like ICRF Antenna (ILA) as well as the LH launcher are represented. The IR camera view is represented in grey. The A2 antenna A, the ILA and half of the A2 antenna B are in the camera view. The interaction between ICRF antennae and the plasma SOL can lead to hot spots on the A2 antenna septa, and on the poloidal limiters in the vicinity of the antennae (main poloidal limiter, ILA limiters and A2 septa as shown in Figure 1). LH hot spots can also be observed by this camera, for example on poloidal limiter tiles, ILA limiter tiles, A2 septa tiles and upper dump plates.

Figure 2 is an internal picture of JET, showing the LH Launcher, the ICRF A2-antenna B and the ITER Like Antenna. The LH system [9] runs at 3.7GHz, and 6MW of LH power can be launched, using a phased array of waveguide antenna, for a corresponding launched power density of $25\text{MW}/\text{m}^2$. The parallel wave refractive index, $N_{\parallel} = k_{\parallel} / k_0$ is adjustable in the range $1.4 < N_{\parallel} < 2.3$ (k represent wave vector components, \parallel refers to the direction parallel to the magnetic field). The launcher is made of 48 multijunction modules [10] (6 in the vertical direction \times 8 in the horizontal direction), for a total of 384 active waveguides facing the plasma (12 rows in the vertical direction \times 32 waveguides in the horizontal direction). LH power absorption in front of the launcher can generate fast electron beams and lead to the formation of hot spots on PFCs magnetically connected to the launcher [11]. On Figure 2, we have indicated the approximate topology of field lines starting from the bottom rows of the LH launcher and intercepting the ILA-limiter2 on which such LH hot

spots can be observed.

A2 antenna B is also visible in Figure 2. Each A2 antenna [12] is a phased array of 4 poloidal straps; controlling the phase between straps enable launching waves with different k_{\parallel} spectra. Usually, π phasing (referred in this text as dipole phasing) or $\pm \pi/2$ phasing (current drive phasings) between adjacent straps are used. For dipole phasing, the antenna power spectrum is maximum at $|k_{\parallel,0}| \sim 6.6 \text{ m}^{-1}$, while for $\pm \pi/2$ phasings $|k_{\parallel,0}| \sim 3.4 \text{ m}^{-1}$. The plasma facing part of the antennas is covered with a faraday screen consisting of tilted Beryllium rods so that the straps themselves are not visible on Figure 2. Each antenna is surrounded by two poloidal limiters made of CFC. Also each A2 antenna integrates in the middle (between straps 2 and 3) a vertical CFC septum. As will be described in this document, hot spots can develop on these septa when local ICRF power is used. In this paper we present analysis results for A2 antenna A septum, but similar heat fluxes and behaviour are observed on antenna B. A2 antennae A and B are fed by the same RF amplifiers, through a 3dB hybrid coupler system.

The IR system is described in [7] and an IR image is shown in Figure 4. The IR camera wavelength measurement range is $3.97\text{--}4.00\mu\text{m}$. The spatial resolution of the camera is approximately 3.5cm at distances corresponding to the ILA limiters. In most of the pulses described here the camera time resolution is 16ms (60Hz acquisition rate) and the exposure time is $300 \mu\text{s}$. One possible source of uncertainty is the surface emissivity which was here assumed to be 0.8 (carbon).

3. DECONVOLUTION METHOD TO DETERMINE HEAT FLUXES FROM IR SURFACE MEASUREMENTS

As on JET the heating pulse lengths are at best of the same order as the typical thermal time constants of the inertial PFCs (thermal equilibrium not reached) a deconvolution of dynamical temperature evolution is necessary. The procedure used to analyse PFC surface temperature measurements in order to evaluate the heat fluxes as a function of time is adapted from [6], [13] and [14] and it is illustrated for few time steps in Figure 3. We assume that the thermal system is linear (this assumption holds if flux variations are not too large) and that the thermal response does not evolve over time. We define the heat load at one location by $Q(t)$. $Q(t)$ is typically a maximum or an averaged heat flux over the heat pattern. In order to fully characterize $Q(t)$, one needs to follow the time trace of the surface temperature $T(t)$ (typically the maximum temperature of a hot spot, or spatially averaged over a hot zone). For ($t < t_0$) it is assumed that the applied flux is null and the object temperature is T_0 . For the numerical analysis, time is sliced into N sequences with $\Delta t = t_i - t_{i-1}$ (time points typically correspond to IR camera acquisition period). The thermal load is represented as a juxtaposition of constant fluxes Q_i , between t_{i-1} and t_i , the applied heat flux is:

$$Q_i = \sum_{j=1}^i \Delta Q_j \quad (3.1)$$

where ΔQ_j represents a flux increment between time sequences $j-1$ and j .

We define $F(t)$ as the thermal response of the object to be analysed to a reference Heaviside excitation applied from $t=0$ (flux is null before $t=0$ and equal to a unit power density afterwards). Ideally $F(t)$ should be measured in controlled conditions. In our case, it is derived from thermal simulations (response to a heat step). The temperature T_i at the end of sequence i is:

$$T_i = T_0 + \Delta T_i \quad (3.2)$$

with

$$\Delta T_i = T_i - T_0 = \sum_{j=1}^i \Delta Q_j F(t_i - t_{j-1}) \quad (3.3)$$

Then, using the measurements by identifying ΔT with ΔT_{IR} , calculating the flux increments Q_j is just a matter of matrix inversion

$$\Delta Q = M^{-1} \Delta T = M^{-1} \Delta T_{IR} \quad (3.4)$$

where

$$\Delta Q = \begin{bmatrix} \Delta Q_1 \\ \Delta Q_2 \\ \dots \\ \Delta Q_N \end{bmatrix} \quad (3.5)$$

and

$$M = \begin{bmatrix} F(t_1 - t_0) & 0 & \dots & 0 \\ F(t_2 - t_0) & F(t_2 - t_1) & \dots & 0 \\ \dots & \dots & \dots & \dots \\ F(t_N - t_0) & F(t_N - t_1) & \dots & F(t_N - t_{N-1}) \end{bmatrix} \quad (3.6)$$

Various modelling tools can be used to describe the thermal response of the tiles. We used extensively the ANSYSTM [15] finite element software taking into account the 3D geometry of the tiles, the anisotropy of the thermal properties of CFC and the temperature dependent properties of the CFC (Dunlop 704/708 CFC); the heat fluxes applied in the reference simulations to calculate $F(t)$ were of the same order of magnitude as the heat fluxes we wanted to evaluate, and the start temperature T_0 matched the measurements.

We shall conclude this section with general remarks. Heat flux evaluation from temperature measurements is an inverse heat conduction problem, and depending on details in material properties, geometry and boundary conditions, a wide range of heat fluxes can lead to the same surface temperature response [13]. Assumptions associated with different models need to be carefully

evaluated because they can lead to huge differences in the evaluated heat-fluxes whilst still giving a good explanation of the measured surface temperature. For each model, the deconvolution is always able to produce a $Q(t)$ that perfectly matches a given $T(t)$, although the result might not be physically reasonable (e.g. negative fluxes might come out). The models therefore need assessment. For that purpose it is common to use the cooling down at the end of the pulse. We are primarily interested in wave-induced power dissipation, so that $Q(t) = 0$ can be expected when the wave power is off. Then the cooling-down of the tile is driven only by its thermal properties and boundary conditions. We have used extensively this phase to check the quality of our thermal models either by verifying that $Q(t)$ obtained from the deconvolution procedure be close to 0 when wave power is off, or by imposing $Q(t) = 0$ after application of wave power, and verifying that the simulated temperature obtained from equation (3-3) follows the measured (IR) temperature. In the next sections, we describe thermal models of tiles where hot spots develop when using ICRF or LH wave heating and current drive systems. We take into account the tiles geometry, their physical properties, and the heat flux pattern. We calculate the reference thermal responses $F(t)$ from these models and we use the surface temperature deconvolution method to evaluate time dependent heat-fluxes.

4. HOTSPOTS ON PFCS SURROUNDING ICRF ANTENNAS FROM RF SHEATH RECTIFICATION.

4.1 RF HOT SPOTS OBSERVATION

When using ICRF waves, hot spots observed on the antennae structure and on limiters close to the powered antennae, can be explained by enhanced heat loads due to acceleration of ions in RF-rectified sheath potentials [16]. These hot spots are visible in Figure 4 for a pulse in which 3MW of ICRF power is launched from A2 antennae A and B. The maximum surface temperature of septum A is $\sim 600^{\circ}\text{C}$, ($T \sim 400^{\circ}\text{C}$). For comparison, in a reference pulse with the same plasma configuration and same amount of ICRF power launched from A2 antennae C and D (and same antenna strap phasing), these hot spots are not visible and the surface temperature increase of septum A during application of ICRF is less than 10°C . A first attempt to characterise these heat loads was reported in [17]. We shall here use a more elaborate thermal model of the tiles subjected to local ICRF heat loads. The so called RF hot spots are located in the shadow of the poloidal limiters surrounding the antennae, and there is some evidence that they correspond to locations where a deposit has developed throughout the operation of JET since the installation of these tiles in 1994. In particular, such deposit can be seen on pictures of the tiles taken during the 2010 shutdown (see Figure 5). More recent visual observations suggest that at some locations, the material of the tile itself has experienced degradation at the surface, probably due to intense exposure to heat flux (these heat loads are most likely due to a combination of operating conditions with plasmas with high energy content and small separatrix-septum distance, and are probably not caused by local RF sheath rectification studied here). Moreover, the time constant associated with temperature increase/decrease of the RF hot spots when turning ON/OFF the local ICRF power is short. This can hardly be explained by

thermal models of the tiles without introducing a layer of material with poor thermal conductivity at the surface of the component.

4.2 SIMPLE MIXED 1D/3D MODEL OF THE A2 SEPTUM TILES

A simple way to model the thermal response of a tile with a deposit or a degraded layer at its surface is using a 1D modelling as is sketched in Figure 6. We assume that on the surface of the tile there is a layer of material which has physical and thermal properties different from those of the tile bulk (typically, with poor thermal conductivity). This 1D approach is justified because the thickness of the deposit is small in comparison with the dimension of the heat pattern. To obtain the temperature response to thermal stimulation, the heat diffusion equation is solved numerically using a finite difference scheme [18], in a plate including a bulk characterised by $(x_{\text{bulk}}, \kappa_{\text{bulk}}, \rho_{\text{bulk}}, C_{p_{\text{bulk}}})$ and a thin layer characterised by $(x_{\text{layer}}, \kappa_{\text{layer}}, \rho_{\text{layer}}, C_{p_{\text{layer}}})$, where x is the material thickness, κ is the thermal conductivity, ρ is the mass density, and C_p is the specific heat capacity. For simplicity, the layer parameters are assumed constant with temperature. To take into account the real 3D properties of the CFC tile, we have run ANSYSTM reference simulations of the thermal response of the tile (without surface layer), as illustrated in Figure 7. In the 1D model without deposit, we have adjusted the bulk physical properties, with ad-hoc $(x_{\text{bulk}}, \kappa_{\text{bulk}}, \rho_{\text{bulk}}, C_{p_{\text{bulk}}})$ parameters in order that the 1D bulk temperature response when exposed to a flux of 1MW/m^2 reproduces well the ANSYS modelling with the tile exposed to the same flux intensity (typical response time $\sim 5\text{s}$).

4.3 SURFACE LAYER PARAMETERS ADJUSTMENT IN THE 1D MODEL

Once the bulk properties of the 1D model are set, the layer parameters are adjusted so that the modelled fast response when the tile is cooling down matches well the measured surface temperature assuming that the applied flux is null when the ICRF power is OFF. We have verified that this fast surface temperature response of the surface layer only depends on the reduced parameters (see appendix A or [19]):

$$\tau_{\text{layer}} = \frac{x_{\text{layer}} \times \rho_{\text{layer}} \times C_{p_{\text{layer}}}}{a_{\text{layer}}} \quad (4.1)$$

$$\alpha_{\text{layer}} = \frac{\kappa_{\text{layer}}}{x_{\text{layer}}} \quad (4.2)$$

τ_{layer} is the characteristic thermal response time of the surface layer (typical response time $\sim 2\text{s}$ or less), and α_{layer} is the deposit thermal conductance similar to the one defined in [20]; in quasi-static conditions, the temperature increase across the surface is proportional to the heat flux: $\Delta T_{\text{layer}} = Q / \alpha_{\text{layer}}$.

An example of analysis is illustrated in Figure 8 where the heat flux is estimated at location of septum A indicated in Figure 4 (this location is in the region on the septum receiving the maximum power load) for Pulse No: 79799 (L mode plasma, 1.5MW launched from A2-A and 1.5MW launched

from A2-2, $\pi/2$ phasing). Results from the surface temperature deconvolution procedure are shown for three cases, where different deposit parameters were considered in the 1D model used to calculate the reference $F(t)$ thermal responses. In all three cases, the fast cool-down of the tile can be well reproduced ($24s < t < 25.5s$), but only case (b) can reproduce both the slow and the fast cool-down. In case (a), the heat-flux is underestimated ($\alpha_{\text{depos}_{(a)}} < \alpha_{\text{depos}_{(b)}}$ therefore $Q_{\text{estimate}_{(a)}} < Q_{\text{estimate}_{(b)}}$ for same measured ΔT), and consequently the estimated temperature for $t > 26s$ is too low. In case (c), the heatflux is overestimated ($\alpha_{\text{depos}_{(c)}} > \alpha_{\text{depos}_{(b)}}$ therefore $Q_{\text{estimate}_{(c)}} > Q_{\text{estimate}_{(b)}}$ for same measured ΔT), which leads to overestimation of the tile surface temperature for $t > 26s$.

In summary, the long time scale cool-down of the tile ($t > 26s$ in Figure 8) is essentially determined by the bulk properties and the flux intensity applied during the heating period while the fast cool down of the tile is function of τ_{depos} , α_{depos} and of the applied heat-flux intensity. Consequently, the absolute heat flux evaluated using this method does not critically depends on the fine details of the modelled deposit properties. Rather, it will depend on the boundary conditions considered in the ANSYS reference simulations of the tile (adiabatic condition or fixed temperature of the back face, the size of the heat pattern, etc). These different boundary conditions lead to a 20 % uncertainty in the intensity of the estimated heat fluxes, the error bars in Figure 8-b account for this uncertainty.

In practice, we do not expect that the layer properties at the tiles surface are uniform along the septum, we have therefore implemented the following method to evaluate the heat flux at any location on the septum:

- Run 10×10 simulations to have the corresponding $F(t)$ reference function populating the space $0 < \tau_{\text{layers}} < 2s$ and $0.5 \times 10^3 < \alpha_{\text{layer}} < 5 \times 10^3 \text{Wm}^{-2}\text{K}^{-1}$
In the deconvolution procedure force the flux to zero when ICRF is Off.
- Run the deconvolution procedure with all the $F(t)$ reference functions and calculate the error function:

$$\text{error} = \sum_i |T_{\text{evaluated}}(t_i) - T_{\text{IR}}(t_i)|, \text{ with } T_{\text{evaluated}} \text{ from equation (3-3).}$$

The main contribution to the error function comes from time points where ICRF is OFF (the purpose of the deconvolution procedure is to adjust the heat flux so that $E_{\text{evaluated}} = T_{\text{IR}}$ except flux forced to zero during cooling down), ie from the differences in the cooling down between the model and the measurements.

- We retain the case which minimise the error function as the ‘best’ evaluation of the heat flux.

4.4 DISCUSSION ON MODELLING RESULTS

For case (b) in Figure 8, which best explains IR measurements, when ICRF power is applied the estimated heat flux varies between 0.35 and 0.6MW/m^2 . Similar heat flux variations are observed on the antenna B septum, and also on the ILA limiter when A2 antennae A and B are powered. These variations might be caused by slight variations of the electron density in front of the antenna which

could change the loading conditions and the electromagnetic field distribution right in front of the antenna, or by a redistribution of the electric field between antennae A and B which are fed by common RF amplifiers through 3dB hybrid couplers, and largely connected magnetically.

The deposit parameters used in this case are $\tau_{\text{layer}} = 1.75\text{s}$ and $\alpha_{\text{layer}} = 2 \cdot 10^3 \text{Wm}^{-2}\text{K}^{-1}$. If we assume that the physical properties of the deposit are close to those of pyrolytic graphite ($\rho_{\text{graph}} \sim 2.2 \times 10^3 \text{kgm}^{-3}$, $C_{p_{\text{graph}}} \sim 1.6 \times 10^3 \text{JK}^{-1}\text{kg}^{-1}$), one can infer from this model $x_{\text{depos}} \sim 1\text{mm}$, which is compatible with recent observation of deposits with a fraction of mm thickness on A2 septum tiles removed from JET during the 2010 shut-down. We have verified that the layer parameters in our model in order to best explain IR measurements are consistent from pulse to pulse. Also, in general location where we observe thick layers correspond to higher values of τ_{layers} and α_{layer} . More analysis are planned in order to better characterise the surface of the CFC A2 antenna septum tiles, and in particular better determine the thickness of the deposit and depth of the degraded CFC layer. However, it should be noted that the surface of some septum tiles have been recently analysed using Ion beam Analysis. This analysis has revealed that the deposit observed in the shadow of the tiles is made of a substantial fraction of Beryllium (up to 15 % of atomic content). The IR emissivity of this layer including metal might be lower than the 0.8 value assumed for carbon, which would lead to a proportional underestimation of the heat-fluxes.

5. INTENSITY OF RF HOT SPOTS VS ICRF SYSTEM AND SOL PLASMA PARAMETERS

We have applied the surface temperature analysis method to determine the heat flux on Antenna A septum (at location indicated in Figure 4), in a series of L-mode pulses ($I_p = 2\text{MA}$, $BT = 2.7\text{T}$, ICRF Frequency: 42MHz , (H)D plasma with $\sim 5\%$ minority specie) in which only the following parameters were changed from pulse to pulse:

- Power balance between antennae A&B vs C&D (with the total ICRF power was kept to 3MW), the average forward voltage in the transmission lines feeding antenna A was in the range $0\text{-}11\text{kV}$.
- Antenna-separatrix distance and thus mainly electron density right at septum position (RF voltage applied to antennas also slightly changes when changing antenna-separatrix distance to compensate for the change in coupling resistance as the system is configured to maintain a target launched power). The density measured by the edge reflectometer at $R = 3.882\text{m}$ (position of the main limiters in the mid-plane) was in the range $[1\text{-}2.6]10^{18} \text{m}^{-3}$.
- Strap phasing.

In Figure 9 we plot the estimated heat flux on A2-A septum as a function of the product of the RF voltage averaged over the transmission lines feeding the antenna, and the density at the limiters radius: The heat-flux on A2 septum tiles increases linearly with the electron density at the septum position and with the RF voltage in the transmission lines feeding the antenna. This is consistent with simple models of power dissipation through RF sheaths rectification [16], and with some previous

characterisation of the associated heat loads on Tore-Supra [21] and JET [17]. Also, current drive strap phasing leads to higher power dissipation. In general, strap phasing corresponding to smaller values of $k_{\parallel,0}$ lead to higher heat fluxes in accordance with antenna modelling showing enhanced E_{\parallel} (|| component of the antenna electric field) in these cases [22].

Indeed, the maximum heat flux observed on antenna septa from local ICRF power dissipation correspond to following operating conditions:

- Current drive strap phasings ($\pm \pi/2$)
- High local power on the antenna ($> 1.3\text{MW}$)
- Small plasma-antenna distance (separatrix-outer limiter distance in mid plan $\sim 3\text{--}4\text{cm}$).

In these worst case conditions the observed surface temperature of the septa can reach 800°C , and the estimated heat-flux normal to the septa is up to 2 MW/m^2 which corresponds to a heat flux along field lines of approximately 5 MW/m^2 , when taking into account the angle of incidence of the field lines on the septa surface.

6. HOT SPOTS FROM LH ABSORPTION IN FRONT OF THE LAUNCHER

6.1 LH HOT SPOTS OBSERVATION

On Tore-Supra [11], TdeV [4] and JET [23][24] tokamaks, it is observed that a fraction of the LH wave power is absorbed by the plasma directly in front of the grill. This is explained by electron Landau Damping of the waves with high N_{\parallel} ($N_{\parallel}=k_{\parallel}/k_0$) components ($|N_{\parallel}|>15$) directly in front of the grill, generating fast electrons in co and counter current directions with energies up to few keV [25]. These fast electrons experience no perpendicular diffusion on their path (which can be few ten of meters) along the field lines, until they hit a PFC. This mechanism can explain the localised hot spots observed experimentally, and precisely located on JET components magnetically connected to the launcher [24]. Referring to Figure 10 and depending on the plasma configuration and LH launcher radial position, LH hot spots can be observed on the septa of A2 antennae A or B (location 1 and 4), ILA poloidal limiters (2 and 3), main poloidal limiter (5), upper dump plates (6), inner (7) and outer divertor aprons (8), with in some cases connection length of few tens of metres. The hot spots on locations 1 to 7 correspond to electrons accelerated in the co-current direction, while location 8 intercepts electrons accelerated in the counter-current direction. Hot spots at locations 1–5 are generally observed if the bottom rows of the grill are powered. This can be understood from Figure 11: Fast electrons travelling in the co-current direction, and generated in front of the bottom rows of the grill, get closer to the poloidal protections and eventually hit them when travelling from $Z<0$ to $Z>0$ (In experiments in which we want to characterise hot spots on the poloidal limiters, the grill is positioned flush, or few mm in front of the main poloidal limiters). Hot spots are observed on the upper dump-plates (6), only for plasma configurations with a secondary X point on top of the machine, as in Figure 10 and Figure 11. In these cases hot spots 7 are generally not seen, and vice-versa. Figure 12 illustrates that fast electrons accelerated in front of the launcher rows will create a pattern of hot spots, corresponding to the projection of the waveguide rows on the poloidal limiter, following the

field lines as is observed in the IR image (Figure 10). Some work have recently been carried out to better understand the spatial structure of the LH e- beam and characterise the electrons energy (see [24, 26, 27, 28]). In the present paper we should focus on the quantification of the heat loads on PFCs intercepting the LH fast electrons.

6.2 THERMAL MODELLING OF THE LH HOT SPOTS

A thermal model of the LH hot spot on the ILA limiter-2 tiles (where a well defined hot spot pattern can be observed) was developed via 3D finite element simulations with ANSYS™. At this location, the tiles are free of deposit so it was not necessary to include deposited layers with poor thermal conductivity in the modelling. A representation of this model is shown in Figure 13. The intensity of heat-flux normal to the surface is non uniform in the radial (x), vertical (y) and toroidal (z) directions. The heat-flux is assumed to have the following spatial dependence:

$$Q(x, y, z) = Q_0 \left[\cos\left(\pi = \frac{y}{7.2}\right) \right]^2 \cdot f(x, z) \quad (6.1)$$

where y is in cm (y=0 is the centre of the tile). This y dependence of the heat flux corresponds to the pattern of the electric field $E_z(y)$, in front of the waveguides of the LH launcher (see Figure 12), assuming that the fast electrons leaving the LH Launcher have energy proportional to $|E_z(y)|^2$ consistent with the theory of LH wave absorption in front of the launcher [30]. The radial extension of the electron beam intercepting the limiter, x, was estimated by tracking the hot spot on the ILA limiter when the launcher is moved backwards from a position where the launcher is in front of this limiter. The (x,z) dependence of the normal flux on the tile surface reflects the increase of the grazing angle of the field lines on the tile profile when going toward increasing z, and assuming that electron beam intensity is uniform across Δx (coherently with [24]). Once the reference thermal response function F(t) has been obtained from this modelling the LH-hot spot temperature deconvolution procedure described on section 3 was applied to evaluate the heat-flux normal to the tile surface and the power density associated to the fast electron beam generated in front of the grill.

6.3 RESULTS FROM HEAT FLUX EVALUATION

An example of analysis of the bottom hot spot on the ILA limiter is presented in Figure 14-a for Pulse No: 77393 in which LHCD is used between 6s and 12s. 1.9MW was launched from the top rows fed by klystron modules A and B, and 1.05MW was launched from the bottom-left part of the grill fed by klystron modules E, the launched power density was 25MW/m² approximately. The plasma parameters in this pulse were the following: L-mode plasma; $B_T = 2.95$ T; $I_p = 1.75$ MA; $q_{95} = 5$. Gas injection (D2) close to the grill was used (6×10^{21} el/s) to improve antenna coupling. The separatrix grill distance was approximately 9cm, and the grill was retracted in 1 cm steps at 8s and 10s (radial grill position in front of the main poloidal limiter indicated in Figure 14-b). The LH fast electron beams generated from the 4 bottom rows of the grill are intercepted by the ILA limiter

only for the most retracted position (10-12s). Applying the surface temperature deconvolution procedure on the bottom hot spot, local peak heat-flux has been calculated assuming that $x = 7.5\text{mm}$. The parallel heat flux plotted in Figure 14-a is evaluated taking into account the grazing angle of the field lines on the tile. At $t = 11\text{s}$, it is in the range $9\text{-}17\text{MW/m}^2$. The error bars account for the uncertainty in the exact value of x ($5\text{mm} < x < 10\text{mm}$ in this case). The heat flux on the ILA limiter tiles continuously increases during the exposure period. This could be caused by small changes of the field line incidence on the tiles, small changes of the grill position, or changes of SOL conditions ($n_{e,\text{SOL}}, T_{e,\text{SOL}}$) throughout the LH phase. In this plasma configuration, the LH fast electrons following field lines passing in front of the poloidal limiters (not intercepted by the poloidal limiters) hit the upper dump plates, throughout the whole LH phase. The heat flux normal to the upper dump plates is $\sim 0.05\text{MW/m}^2$, it is evaluated using a simple thermal model of the graphite plates constituting the dump plates. In Figure 14-b, we have plotted the heat flux along the field lines when projected onto the plasma mid-plane. In doing so, the poloidal and toroidal expansion of the surfaces evaluated from 3D field line tracing based on the EFIT equilibrium code when going from the mid-plane toward the dump plates (150 surface expansion factor) is taken into account. The parallel heat flux estimated from dump plate analysis is approximately 10MW/m^2 which corresponds well to the ILA limiter analysis. Therefore, both ILA limiter and upper dump plates thermal analysis lead, within uncertainties, to equivalent heat fluxes estimates.

Figure 14-b also illustrates that the heat flux on the dump plates does not importantly decrease when the launcher is retracted by 2cm during the pulse. As discussed in more details in [24], this implies that the radial width of the LH wave absorption layer in front of the launcher is of few centimetres, or more. This observation, compatible with recent measurements of the LH electron beam on Tore Supra [26], is a puzzle for theory as simple absorption models predict that the absorption layer in front of the launcher should be of few millimetres, and led to new modelling work [27][28]. Also the information on the radial width of the LH electron beam combined with its power density allow evaluating the total amount of LH power absorbed through this process: for Pulse No: 77393, and assuming that the beam radial width is 3.5 cm, the LH power transferred to fast electron in front of the grill is estimated to 5% in the plasma current direction. If in addition we assume that a comparable amount of power is transferred to fast electrons travelling in the counter current direction, one can estimate that approximately 10% of the launched LH power is absorbed in front of the grill in this case.

7. INTENSITY OF LH HOT SPOTS VERSUS LH POWER AND SOL PARAMETERS

For the LHCD system operation it is important to minimise the LH wave power absorption in the SOL, in order to guaranty the integrity of the first wall, and to maximise the LH power available for current drive. Toward this goal, we need to identify the main parameters influencing the LH electron beam power density. A systematic study on Tore-Supra presented in [31] led to the following experimental scaling law for the power-flux carried by the LH fast electrons:

$$Q_{\parallel} \propto n_e^{1.15} T_e^{0.59} \langle E_{\text{grill}} \rangle^{1.7} \quad (7.1)$$

This is close to a law of the type $Q_{\parallel} \propto n_e \sqrt{T_e} \langle E_{\text{grill}} \rangle^2$ ($\langle E_{\text{grill}} \rangle$ being the spatially averaged electric field in front of the grill) that could be explained by a simple physical picture: the heat flux is proportional to the number of (thermal) electrons entering the grill aperture region (proportional to $n_e T_e$), and to the average energy increase gained by these electrons in front of the antenna waveguides (proportional to $\langle E_{\text{grill}} \rangle^2$) coherently with the description of the electrons acceleration in the LH antenna electric field [30]. The JET experimental results described here essentially support this proposed scaling law. In Figure 15 and Figure 16, we have characterised the heat flux associated with the LH fast electron beam from the grill bottom row for a data base of pulses with a wide range of operating conditions:

- L-mode plasmas with high or low triangularity shape.
- Plasma-launcher distance in the range 4-9cm.
- PLH,E&F in the range 0.5-1.5MW ($P_{\text{LH, E\&F}}$ represents the LH power launched by the 4 bottom rows of the launcher fed by 8 klystrons, ie 4 klystrons from module E and 4 klystrons from module F).
- Grill position: 0.5 cm +/- 3mm in front of poloidal limiters
- Number of active reduced waveguides in the bottom row between 12 and 28 (3 to 7 multijunctions).
- Reflection coefficient from the 4 bottom rows in the range 0.7% < Rc < 3%.

The heat-flux along the field lines, Q_{\parallel} , is estimated using the method described in section 6; for each pulse of the data-base 3D field line tracing was used to account for the differences in field line incidence on the limiter tiles between the different pulses. In Figure 15, the heat-flux is plotted as a function of $P_{\text{LH, E\&F}}$, the power launched from the four bottom rows. There is a large spread in the measured heat-flux plotted as a function launched power per row. In particular launching 0.5MW can lead to a power flux as large as launching 1.5MW. When using a reduced number of active waveguides, and thus operating at higher launcher LH power density (but reduced total power), the heat-flux is noticeably higher. As illustrated in Figure 16, the heat-flux associated with the LH fast electrons increases more consistently with ρ_{LH} the launched power density in the active waveguides. This gives an experimental illustration of two features revealed by the calculation of electron dynamics in the LH launcher electric field described in [30]:

- Increasing the LH launcher power density and thus the intensity of the parallel electric field in front of the active waveguides increases the efficiency of electron acceleration, in the theory this is quantified by the quasi linear diffusion coefficient in the velocity space being proportional to $\langle E_{\text{RF}} \rangle^2$ ([30]).
- Having a reduced number of active waveguides in a row (4 active multijunction modules) can lead to very intense LH electron beams, consistently with the calculations ([30]) showing a

rapid increase in the electron acceleration process when increasing the number of waveguides, and then a saturation when $N_{\text{waveguide}} \sim 20$.

If the electric field in front of the active waveguides is the driving force for the acceleration process, the total launched power is probably the relevant factor for the density increase in front of the launcher observed when LH is applied, this density increase also leads to an increase in the LH hot spot intensity.

The effects of ρ_{LH} , P_{LH} , and density in front of the grill could be studied in more details in a series of pulses with identical plasma conditions and in which we only varied the LH power and number of active waveguides in the 4 upper rows of the grill (fed by klystron modules A and B). In this series of pulses the Lithium (Li) beam diagnostic which measures the SOL density in the upper region of the plasma is magnetically connected to the active upper rows of the grill as is shown in Figure 17. The estimated heat flux from the fast LH electrons onto the upper dump plates is plotted as a function of ρ_{LH} in Figure 18. The heat flux intensity varies roughly as ρ_{LH}^2 . In two different pulses the same 1.33MW is launched from the top rows, but as already noted, using fewer active waveguides (magenta square) and thus working at higher LH power density leads to a noticeably more intense fast electron beam.

The ρ_{LH}^2 non-linear increase of the power flux intensity is compatible with the Tore-Supra scaling [31] expressed in equation (7-1), taking into account neutral ionization right in front of the grill leading to a local increase of the electron density with LH. Figure 19 illustrates that the electron density measured on field lines passing in front of the active rows of the antenna increases as the launched power is increased (we cannot comment on the SOL temperature evolution as this measurement was not available during these experiments). This feature which has a beneficial effect on antenna coupling, is described in [32] and [33], it is attributed to neutrals ionisation by LH wave power in front of the grill. The heat flux associated with the fast LH electrons scales linearly with $\rho_{\text{LH}} \times n_{\text{e,launcher}}$ (see Figure 20) well in line with the Tore-Supra scaling law [31].

CONCLUSIONS

We have implemented a method to analyse surface temperature measurements and evaluate the heat flux on JET plasma facing components, and applied it to the study of hot spots generated by the absorption of ICRF and LH waves in the SOL. This method is fast and versatile. It can be adapted to a large variety of thermal problems. The relevant thermal information for extracting heat loads from surface temperatures of a given PFC is then fully contained in a response function $F(t)$ that needs to be determined only once before analysing a whole series of pulses. The reference temperature response functions $F(t)$ can be obtained via measurements with controlled heat fluxes (if available) or from the most appropriate thermal modelling tools.

When using ICRF at JET, the large temperature increase observed in the vicinity of antennae is caused by rather low heat fluxes onto a layer with low thermal conductance at the tile surface. In worst case conditions (1.5MW/antenna, current drive phasing, plasma-limiter distance of $\sim 4\text{cm}$) the

observed heat-flux from ICRF interaction with SOL plasma on the A2 antenna septa is $\sim 2 \text{ MW/m}^2$ (heat-flux along field lines $\sim 5 \text{ MW/m}^2$). It will be important to perform equivalent heat flux analysis with the new wall which will be (at least at the beginning of the operations) free of deposit. In most cases, the heat fluxes driven by ICRF sheath rectification is not a limitation for JET operation; however more modelling work and experiments validations are needed in order to be able predict these heat loads on ITER, as reported in [17] and [34] for initial studies. Also it is mandatory to optimise the design of ICRF antenna structures in order to reduce excitation of parallel electric field components which drives local heat loads and impurity production [22, 35].

The LH waves can accelerate electrons in the SOL creating very localised heat loads on PFCs magnetically connected to the grill. The maximum power density along the field lines associated with the LH fast e- beam is evaluated in the range $15\text{-}30 \text{ MW/m}^2$ in the mid-plane. The maximum measured peak heat flux projected on tile surface (as defined in equation 6-1) is $Q_0 \sim 7 \text{ MW/m}^2$ in worst case conditions ($\rho_{\text{LH}} > 20 \text{ MW/m}^2$, high density in front of the grill, large fraction of the fast e- beam intercepted by limiter tiles). However it is worth noticing that the experiments described in this paper, were run specially to study the LH hot spot with the density in front of the grill at least 2 times higher than the optimum required for best wave coupling. Acceleration of fast electrons in front of LH grills should be further studied in next generation launchers which could use the ‘Passive Active Multijunction’ (PAM) technology [36, 37] as proposed for ITER. Control of the density in front of the grill is a key operational factor to limit the amount of LH power absorbed in front of the grill. In addition, the power content in the high $|N_{\parallel}|$ part of the spectrum could be reduced from the antenna design stage, by rounding off the sharp edges of the septa between waveguides at the grill aperture, as was proposed in [38].

The Be tiles of the JET new wall have been designed to sustain the equivalent of a flux of $6 \text{ MW/m}^2 \times 10 \text{ s}$ projected on the surface. Therefore, care will be taken when operating JET with the ITER-like wall: to ensure ICRF and LH operation that preserves the Be wall integrity, a protection system including a new viewing system, real time detection of hot spots and real time control of ICRF or LH power is currently being developed.

Finally we should stress out that for both systems, a compromise is needed in order to maximize antenna wave coupling (and thus power transfer to the plasma) while keeping local temperature increase and impurity production acceptable. Both LH and ICRF heat loads scale unfavourably with the high density necessary to optimise wave coupling. On the other hand, high SOL density allows increasing of the separatrix-antenna distance. Similarly, ICRF antenna coupling resistance is generally higher when exciting low- k_{\parallel} spectra that also develop the highest sheath potentials. For both systems, using gas inlets close to the active antennas can be a knob to control the density in front of the antennae as described in [39] and [40]; In particular one would like to implement real time systems controlling the amount of gas injected locally to reach a target launcher reflection coefficient (or coupling resistance) with the temperature of sensitive areas taken as a constraint.

ACKNOWLEDGMENTS

This work, part-funded by the European Communities under the contracts of Association between EURATOM and CCFE, CEA and other associations listed within the author list, was carried out within the framework of the European Fusion Development Agreement. The views and opinions expressed herein do not necessarily reflect those of the European Commission. This work was also part-funded by the RCUK Energy Programme under grant EP/I501045. One of the authors (V.P.) was supported by the Czech Science Foundation Project No. GACR 202/07/0044.

APPENDIX A

This appendix investigates the thermal behaviour of a thin layer deposited on top of a bulk material. An equivalent development can be found in reference [19]. The model is simplified in that 1°) it is 1D along a spatial coordinate x ; 2°) the thermal attachment of the layer is assumed perfect; 3°) a clear separation of time scales is assumed between the thermal responses of the layer and of the bulk.

The deposit is characterized by its thickness x_{layer} , density ρ_{layer} , massic heat capacity Cp_{layer} , and thermal conductivity κ_{layer} .

For time $t < 0$ the layer as well as the bulk are at uniform temperature T_0 . From $t = 0$ a thermal flux density $Q(t)$ is applied at the front face of the layer ($x = 0$). It is supposed that the thermal response of the layer is far faster than that of the bulk, as well as the characteristic time of variation for the flux $Q(t)$ after $t = 0$. Consequently over the short time scales, the back of the layer ($x = x_{layer}$) remains at the initial temperature T_0 and the flux can be treated as a constant Q . The simplified heat diffusion problem in the layer is therefore summarised as

$$\left\{ \begin{array}{l} \rho_{layer} Cp_{layer} \partial_t T = \partial_x \kappa_{layer} \partial_x T \\ T(x, t = 0) = T_0 \\ -\kappa_{layer} \partial_x T(x = 0, t) = Q ; t \geq 0 \\ T(x = x_{layer}, t) = T_0 \end{array} \right. \quad (A.1)$$

The thermal problem can be made non-dimensional by the following re-scaling

$$\left\{ \begin{array}{l} x^* = x / x_{layer} \\ T^* = \frac{(T - T_0) \alpha_{layer}}{Q} \\ t^* = \frac{t}{\tau_{layer}} \end{array} \right. \quad (A.2)$$

with

$$\left\{ \begin{array}{l} \alpha_{layer} = \frac{\kappa_{layer}}{x_{layer}} \\ \alpha_{layer} = \frac{x_{layer}^2 \rho_{layer} C_{P_{layer}}}{\kappa_{layer}} = \frac{x_{layer} \rho_{layer} C_{P_{layer}}}{\alpha_{layer}} \end{array} \right. \quad (A.3)$$

The dimensionless heat diffusion problem in the deposit is valid for any layer and reads:

$$\left\{ \begin{array}{l} \partial_{t^*} T^* = \partial_{x^*}^2 T^* \\ T^*(x^*, t^* = 0) = 0 \\ \partial_{x^*} T^*(x^* = 0, t^*) = -1 ; t^* \geq 0 \\ T^*(x^* = 1, t^*) = 0 \end{array} \right. \quad (A.4)$$

In particular for $t \gg \tau_{layer}$ one obtains the steady-state solution for the temperature profile

$$T^* = 1 - x^* \quad (A.5)$$

In these expressions Q/α_{layer} is a characteristic steady-state temperature elevation over the layer, while τ_{layer} is the characteristic heat diffusion timescale over the layer thickness. Two layers exhibiting the same τ_{layer} and α_{layer} produce the same surface temperature history $T_{surf}(t)$ when subject to the heat load Q . Therefore they cannot be distinguished from thermographic measurements. When considering timescales longer than τ_{layer} the deposit adds a temperature elevation Q/α_{layer} to the surface temperature of the bulk. Therefore at these long timescales the effect of non-ideal thermal attachment, characterised by its thermal conductance H_c (additional temperature offset Q/H_c) cannot be distinguished from a larger thickness of the layer and can be incorporated in the value of α_{layer} . Neglecting the surface temperature offset from the layer (or more generally over-estimating α_{layer}) leads to over-estimation of the applied steady-state heat fluxes (see Figure 8).

REFERENCES

- [1]. F. Durodié, et al., ‘Latest Achievements of the JET ICRF Systems in View of ITER’, Proc. of the 23rd IAEA Fusion Energy Conference 2010, Daejeon, Korea, EXW/P7-04
- [2]. M.-L. Mayoral, et al., in RF Power in Plasmas, AIP Conf. Proc. 1187, pp 39-46 (2009)
- [3]. M. Bures, et al., Plasma Physics and Controlled Fusion **33** No. 8 pp 937-967 (1991)
- [4]. J. Mailloux, et al., Journal of Nuclear Materials **241-242** p745 (1997)
- [5]. C.E. Thomas Jr, et al., Journal of Nuclear Materials **220-222** p531 (1995)
- [6]. G. F. Matthews, et al., Physica Scripta T138 014030 (2009)
- [7]. E. Gauthier, et al., Fusion Engineering and Design **83** 1335-1340 (2007)
- [8]. J.-L. Gardarein, et al., Fusion Engineering and Design **83** pp 759-765 (2008)
- [9]. J.-M. Noterdaeme, L.-G. Eriksson, M. Mantsinen, M.-L. Mayoral, D. Van Eester, J. Mailloux, C. Gormezano, T. T. C. Jones, Fusion Science and Technology **53** 1103-1151 (2008)

- [10]. X. Litaudon and D. Moreau, *Nuclear Fusion* **30** (3), 471-484 (1990)
- [11]. M. Goniche, et al., *Nuclear Fusion* **38** (6), 919-937 (1998)
- [12]. A. Kaye, et al., *SOFE Conf. Proc.*, 16th IEEE/NPSS Symposium, Vol. 1 p736 (1995)
- [13]. J. Beck, B. Blackwell and C. St. Clair, *Inverse Heat Conduction - Ill-Posed Problems*, Wiley-Interscience Publication, 1985
- [14]. J.-L. Gardarein, *Analyse par thermographie infrarouge de la puissance déposée sur des surfaces recouvertes de carbone dans les tokamaks*, Ph.D. Thesis, Université de Provence Aix-Marseille 1 (2007).
- [15]. ANSYS™, ANSYS Inc., Canonsburg, PA 15317, USA.
- [16]. F.W. Perkins, et al., *Nuclear Fusion* **29** No.4 pp.583-592 (1989)
- [17]. L. Colas, et al., in *RF Power in Plasmas*, AIP Conf. Proc. 1187, pp 133-136 (2009)
- [18]. M. Necati Ozisik, *Finite Difference Methods in Heat Transfer* (CRC Press, Boca Raton, FL, 1994)
- [19]. H.S. Carslaw and J. C. Jaeger, *Conduction of Heat in Solids*, Oxford University Press (1959)
- [20]. P. Andrew, et al., *Journal of Nuclear Materials* **313–316** (2003) 135–139
- [21]. L. Colas, et al., *Nuclear Fusion* **46**, pp. S500-S513 (2006)
- [22]. V. Bobkov, et al., in *RF Power in Plasmas*, AIP Conf. Proc. 1187, pp 221-224 (2009)
- [23]. K. Rantamäki, et al., *Plasma Physics and Controlled Fusion* **47** pp1101-1108 (2005)
- [24]. P. Jacquet, et al., in *RF Power in Plasmas*, AIP Conf. Proc. 1187, pp 399-402 (2009)
- [25]. V. Fuchs, et al., *Physics of Plasmas* **11** p. 4023 (1996)
- [26]. G. Gunn, et al., *Journal of Nuclear Materials* **390–391** (2009) 904–906
- [27]. V. Fuchs, et al., in *RF Power in Plasmas*, AIP Conf. Proc. 1187, pp 383-386 (2009)
- [28]. V. Petržílka, et al., 36th EPS Conf. on Plasma Phys. Sofia, ECA Vol.33E, P4.207 (2009)
- [29]. D.M. Pozar, *Microwave Engineering* (Addison-Wesley, Reading, MA, 1990)
- [30]. V. Fuchs et al., *Nuclear Fusion* **43** pp 341-351 (2003)
- [31]. M. Goniche, et al., *Plasma Physics and Controlled Fusion* **46** (2004) 899–923
- [32]. M. Goniche, et al., *Plasma Physics and Controlled Fusion* **51** (2009) 044002 (18pp)
- [33]. V Petržílka, et al., ‘JET SOL ionization at LH wave launching’ submitted to *Plasma Physics and Controlled Fusion*
- [34]. L. Colas, et al., *Journal of Nuclear Materials* **390–391** (2009) 959–962
- [35]. A. Mendes, et al., *Nuclear Fusion* **50** (2010) 025021 (17pp)
- [36]. P. Bibet, et al., *Nuclear Fusion* **35** (10), 1213-1223 (1995)
- [37]. A. Ekedahl, et al., *Nuclear Fusion* **50** (2010) 112002 (5pp)
- [38]. P. Jacquet, Y. Demers, et al., ‘Effect of septa shape and plasma density on electric field spectra of LH antennas’, CCFM internal report 474e, Centre Canadien de Fusion Magnétique, Varennes, Canada, September 1997.
- [39]. M.-L. Mayoral, et al., ‘On Maximizing the ICRF Antenna Loading for ITER plasmas’, Proc. of the 23rd IAEA Fusion Energy Conference 2010, Daejeon, Korea, ITR/P1-11.
- [40]. A. Ekedahl, et al., *Plasma Physics and Controlled Fusion* **51** (2009) 044001 (17pp)

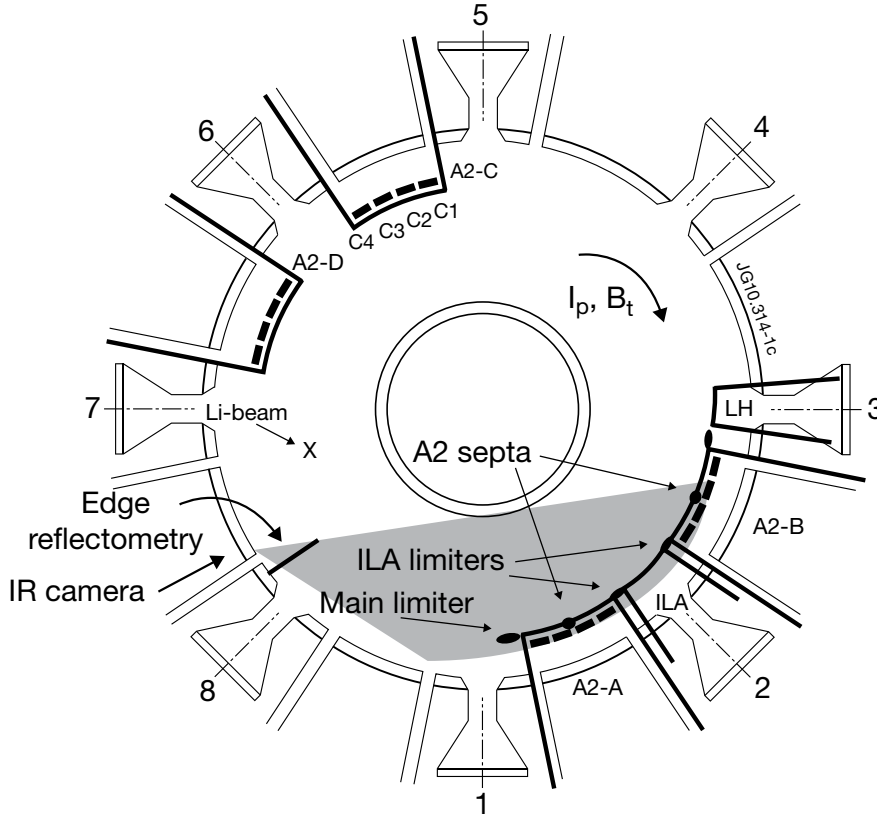


Figure 1: Top view of the JET tokamak showing the four A2 ICRF antennae (A, B, C, D), the ICRF ITERLike Antenna (ILA) and the LH launcher. The IR camera view is indicated in grey. The poloidal limiters and antenna septa seen by the camera are indicated with arrows. The line of sight of the edge reflectometer (close to plasma midplane) and of the Li-beam diagnostic (vertical line of sight on top of the machine) are also shown.

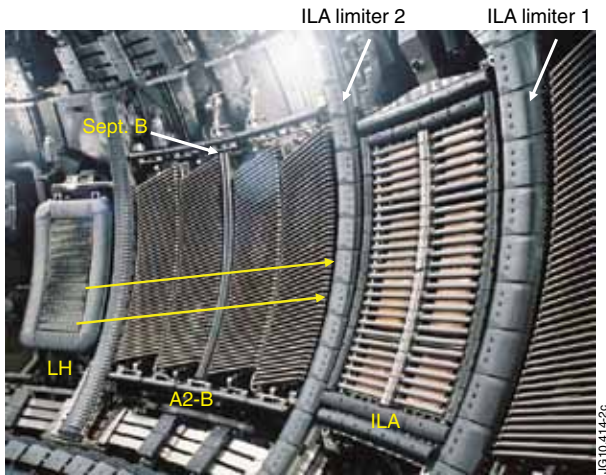


Figure 2: Photo of JET showing the LH launcher, A2 ICRF antenna B, and the ILA antenna. The septum of A2-B and the poloidal limiters surrounding the ILA can be seen. Field line topology from the bottom rows of the LH launcher to ILA-limiter2 (where LH hot spots are often observed) is indicated.

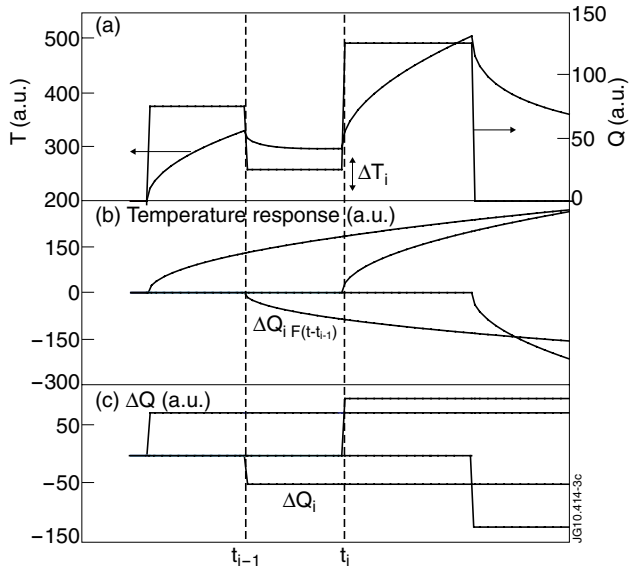


Figure 3: Illustration of the surface temperature deconvolution method to evaluate heat-fluxes. On (a) the heat flux which is the superposition of Heaviside functions is represented (right axis), along with the temperature response. The temperature responses to each Heaviside excitations are represented in (b) and (c) respectively.

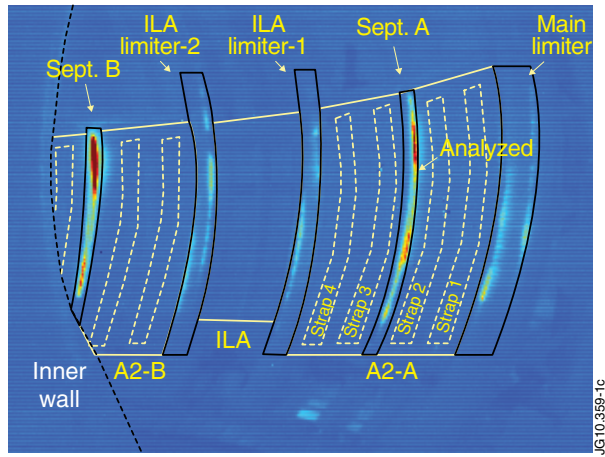


Figure 4: IR image, Pulse No: 79799, $t=23s$. Superimposed are the A2 antennae A and half of B, the ILA, the main and ILA poloidal limiters, and the A2 antenna septa. The location (on septum A) where analysis of the surface temperature was carried-out is shown. In this pulse, only A2 antennae A and B are used, launching 3MW.

(a)



(b)

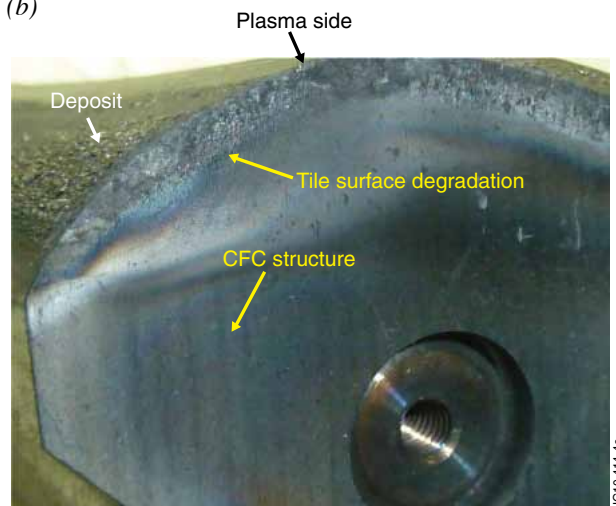


Figure 5: (a) Magnified photo of the plasma facing side of a septum tile from A2 antenna A (at location where heat flux was evaluated). A deposit can be distinguished on the shadow of the tile. (b) Top view of the tile. The deposit at the surface can be distinguished. Also the CFC tile seems to have experienced a degradation of its plasma facing side.

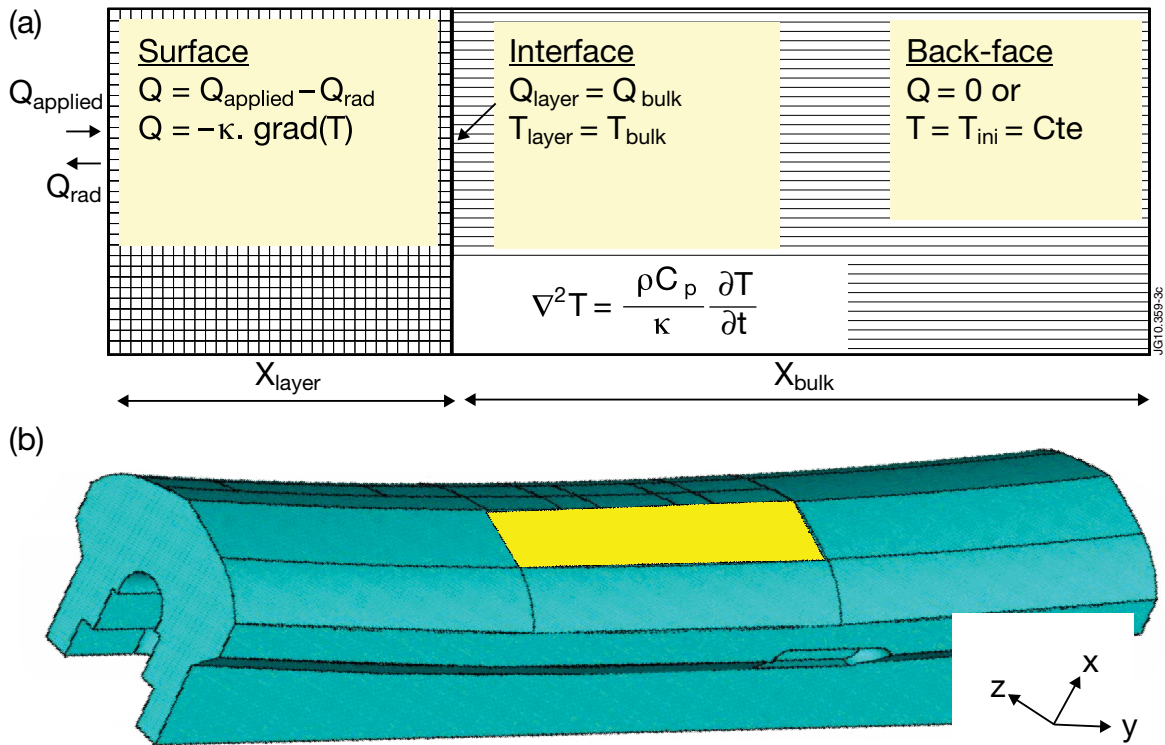


Figure 6: (a) Schematic of the 1D model including a deposit. The heat diffusion equation is solved numerically with a finite difference scheme; boundary conditions are highlighted in yellow. (b) Schematic of a septum tile illustrating a reference ANSYS simulation. The heat flux pattern is applied on the yellow patch.

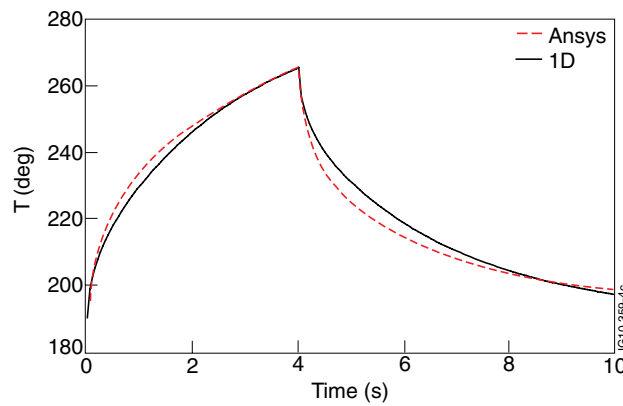


Figure 7: Picture illustrating a reference ANSYS simulation. The boundary condition at the back face is $T_{back}=cte=T_{initial}$. The surface temperature response of the hot spot when applying $1MW/m^2$ (between 0 and 4s) in the ANSYS simulation and in the 1 D simulation (without deposit) are shown.

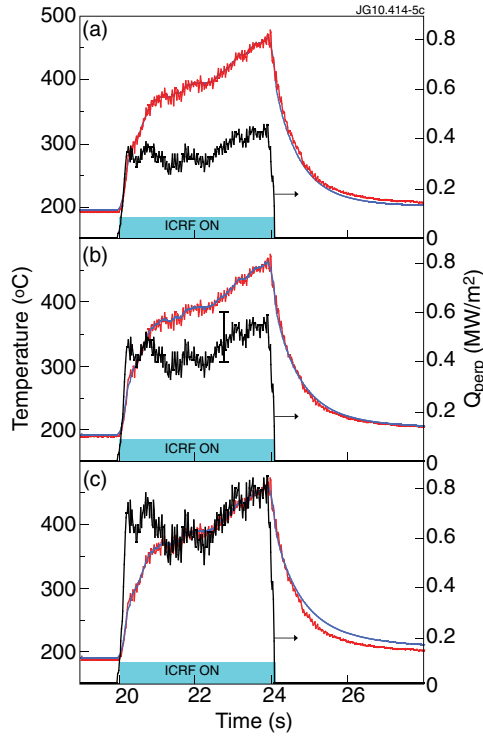


Figure 8: Pulse No: 79799, estimate of applied heat-flux on antenna A2-A septum (at location shown on Figure 4). The estimated flux (black curve) is on the right axis. The surface temperature, measured (red curve) or estimated (blue) from equation (3-3) is on the left y axis. We imposed $Q_{\perp} = 0$ for $t > 24$ s. Results are shown for the three different deposit parameters. In (a), $\tau_{\text{layer}} = 1.75$ s and $\alpha_{\text{layer}} = 1.5 \times 10^3 \text{ Wm}^{-2} \text{ K}^{-1}$. In (b), $\tau_{\text{layer}} = 1.75$ s and $\alpha_{\text{layer}} = 2 \times 10^3 \text{ Wm}^{-2} \text{ K}^{-1}$. In (c), $\tau_{\text{layer}} = 1.75$ s and $\alpha_{\text{layer}} = 3 \times 10^3 \text{ Wm}^{-2} \text{ K}^{-1}$.

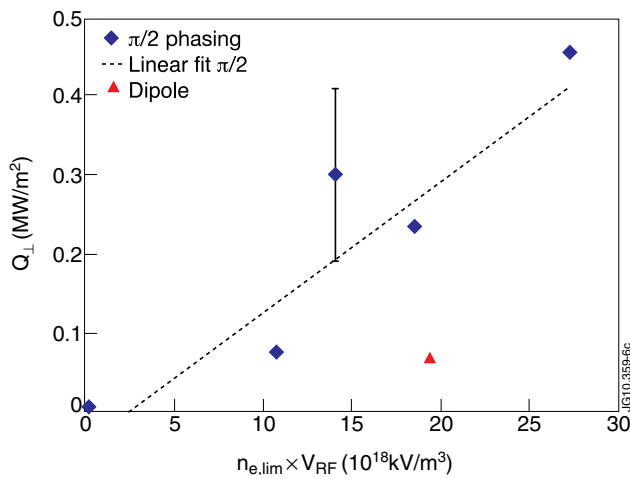


Figure 9: Heat-flux at on antenna A2-A septum (at location shown on Figure 4) versus the product of the SOL density and RF voltage. The SOL density from the edge reflectometer (not directly in front of the antenna) is taken at $R = 3.882$ m (position of limiters at midplane). The RF voltage (averaged over the 4 straps) is measured in the transmission lines feeding antenna A. The error bar is representative of the flux variation during RF. This data set includes Pulse No's: 79797-800 and 79805-806.

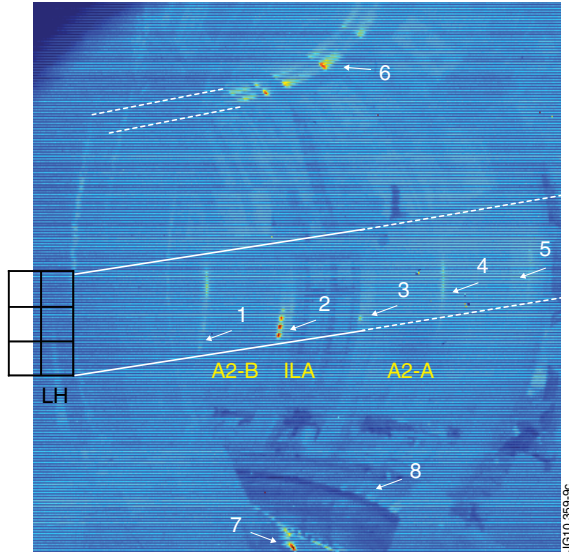


Figure 10: Pulse No: 77393 $t = 12s$, IR image showing where LH hot spots can be observed. The LH launcher is not viewed by the camera but its approximate location is shown. In this pulse the launched LH power density is $\sim 25 \text{ MW/m}^2$, the top 4 rows and bottom 4 rows of the launcher are used. LH hot spots can be seen on the ILA poloidal limiter and on the upper dump plates.

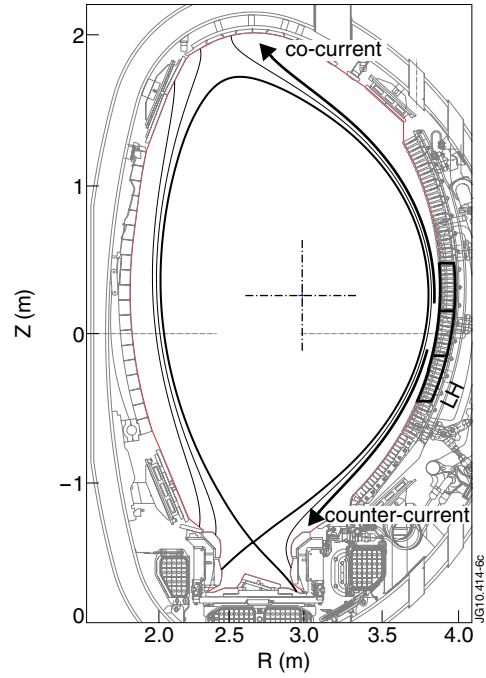


Figure 11: Cross section of plasma, from EFIT equilibrium code, Pulse No: 77393 $t = 10s$.

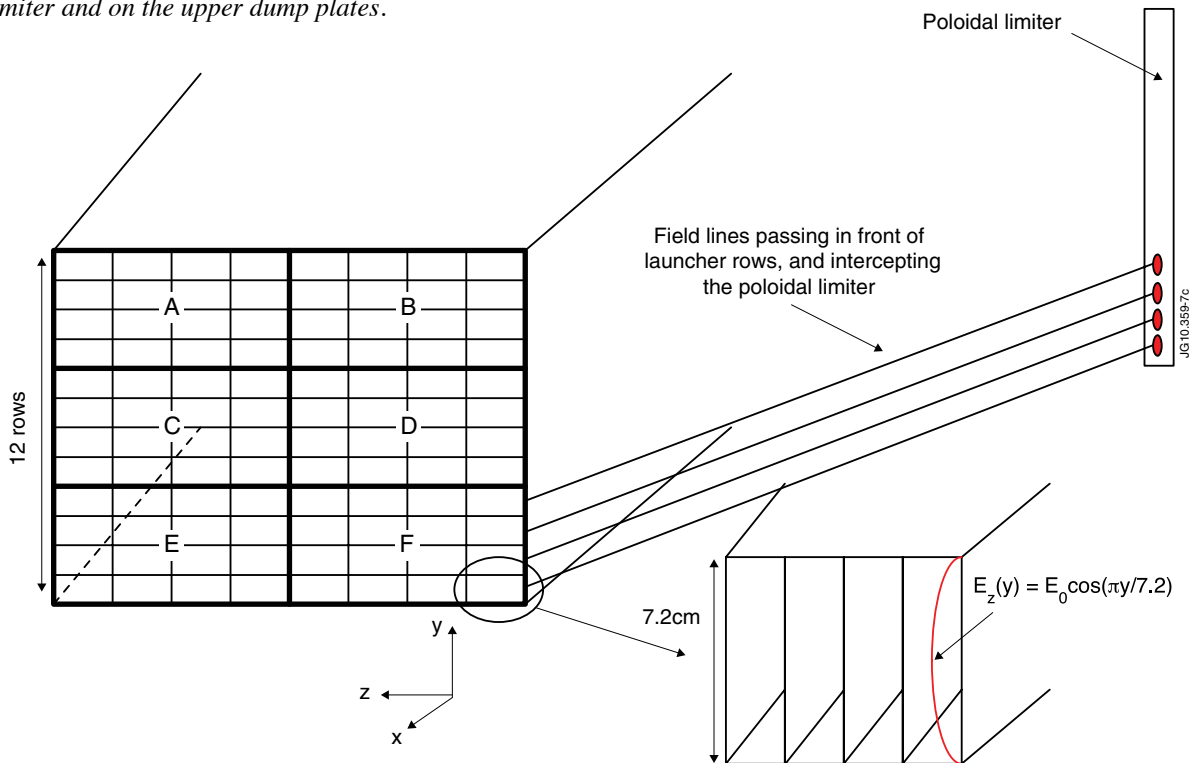


Figure 12: Illustration of LH hot spot formation on poloidal limiters. Hot spot pattern on the limiters is a projection of the grill rows, following the field lines leaving the grill. The $E_z(y)$ electric field dependence corresponds to the $TE_{1,m}$ and $TM_{1,n}$ modes that can be excited at the waveguides aperture [29]. A description of the JET LH system can be found in [9]. The four top rows of the grill are fed by 8 klystrons, A1-4 and B1-4. The four middle rows of are fed by C1-4 and D1-4. The four bottom rows are fed by E1-4 and F1-4.

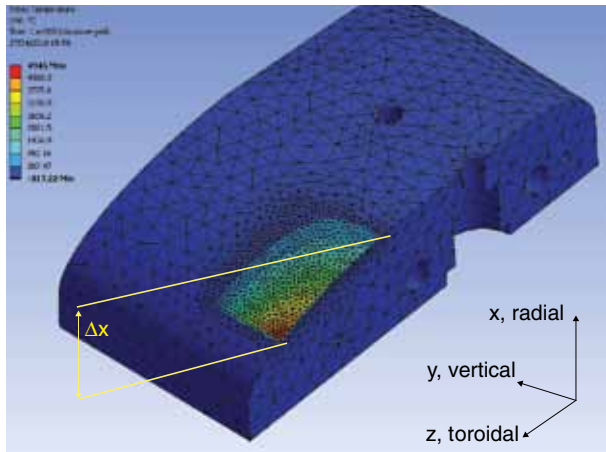


Figure 13: Thermal modelling of an LH hot spot on an ILA limiter tile with ANSYS. Half of the tile and of the hot spot is shown, vertical symmetry is assumed. x is the radial direction, y is the vertical direction, and z is the toroidal direction. CFC fibres are oriented in the (x,z) plan.

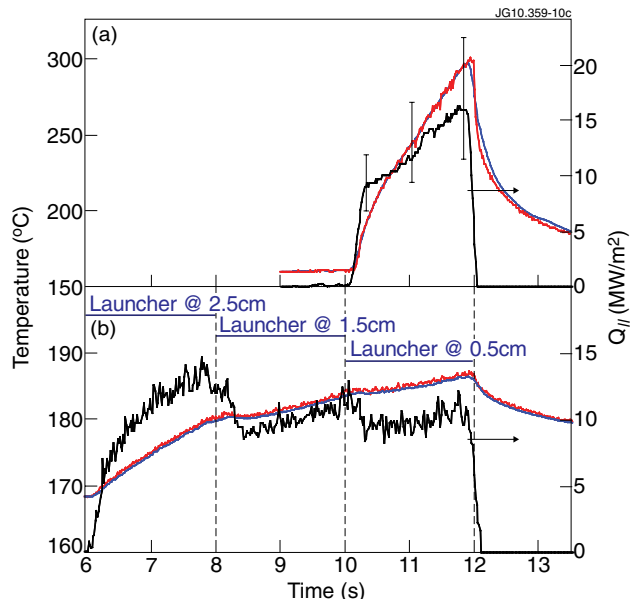


Figure 14: Pulse No: 77393. (a) Evaluation of the peak heat flux along magnetic field-lines associated with the bottom hot spot on ILA limiter. The evaluated heat flux is on the right y axis, and the measured (red) and evaluated (blue) temperatures are on the left y axis. (b) Heat flux along the field lines evaluated from the upper dump-plates temperature evolution, taking into account a flux expansion of 150 from plasma midplane toward the dump plates.

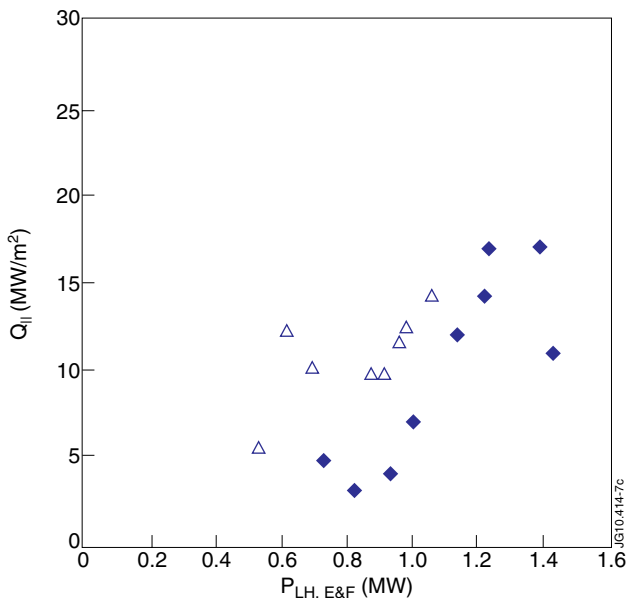


Figure 15: From ILA limiter analysis, heat-flux associated with the fast electron beam from the launcher bottom row (fed by klystron modules E and F), plotted as a function of the launched power from the 4 bottom rows. The open symbols correspond to pulses in which 4 klystrons or less are used to feed the bottom rows.

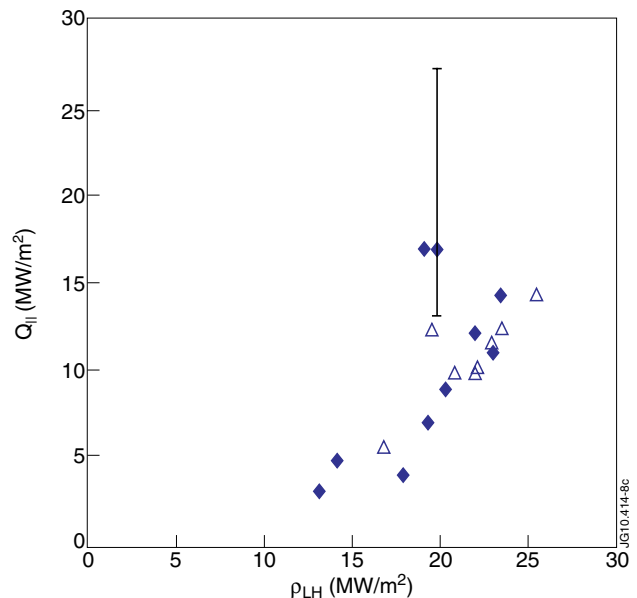


Figure 16: For the same data-set as in Figure 15, the heat-flux is plotted as a function of the launched power density in the 4 bottom row. The error bars describe the uncertainty in the absolute heat-flux values (from uncertainty in exact x value, referring to Figure 13).

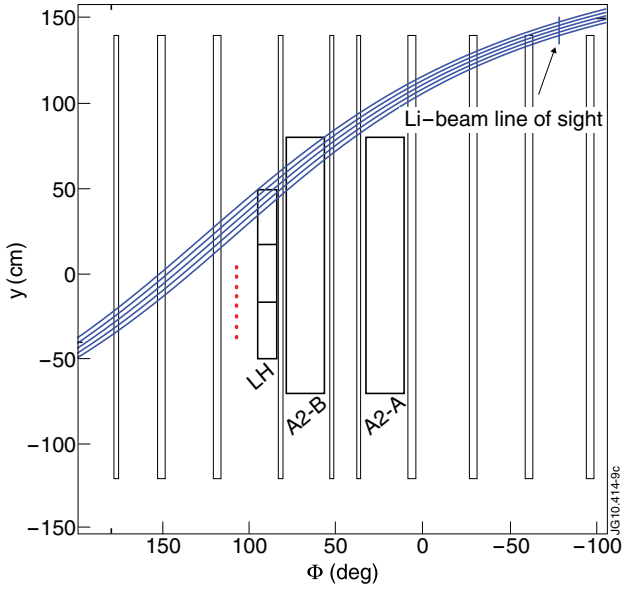


Figure 17: Pulse No: 74540, $t=8s$. Illustration of magnetic connection between the Li-beam diagnostic line of sight, and the LH launcher. The plot is in the toroidal-vertical plan. Looking from the plasma, 4 field lines starting from the Li-beam diagnostic line of sight are shown. Field lines tracing is based on the EFIT equilibrium code.

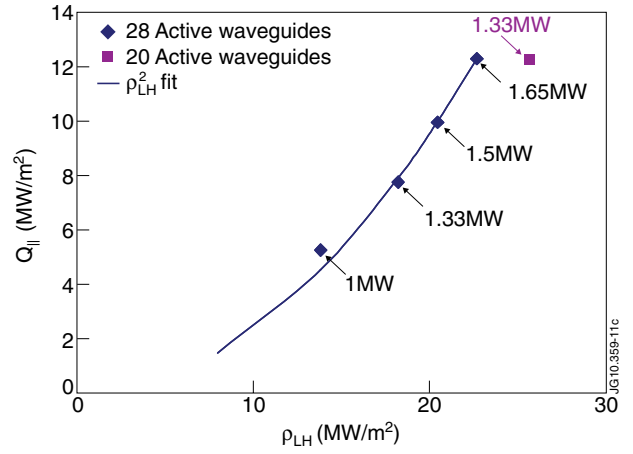


Figure 18. Power flux of LH electron beam from launcher top rows (fed by klystron modules A and B) versus LH power density. Power flux is estimated from upper dump plates analysis and it is projected onto plasma midplane taking into account 3D field line expansion. Data from Pulse No's: 75736-75540, averaged between 8-9s. The labels indicate the total power launched from the 4 top rows.

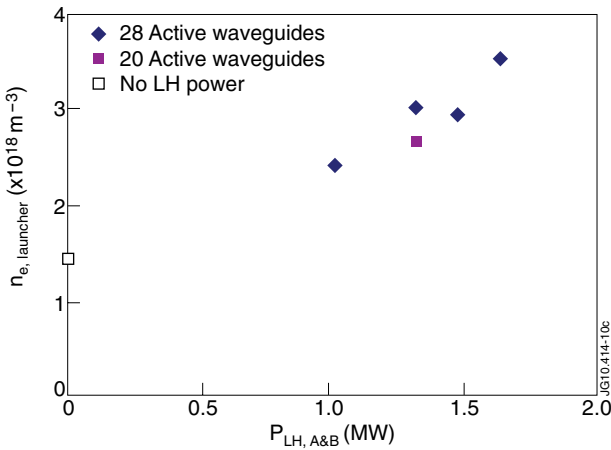


Figure 19: For same data set as in Figure 18, electron density measured by the Li-beam diagnostic is plotted as a function of the launched LH power from the 4 top rows of the launcher fed by klystron modules A and B. The density is the SOL density in front of the launcher, spatially averaged over 2.2cm in front of the grill, $3.858m < R_{MID} < 3.88m$ (measurements mapped on plasma mid-plane, R_{MID} is the radius at mid-plane).

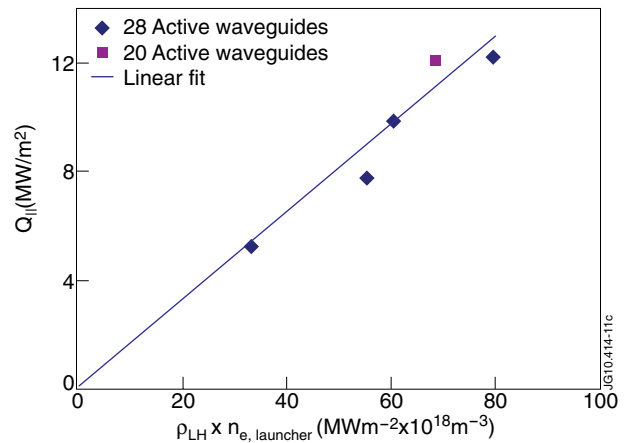


Figure 20: For same data set as in Figure 18, the power flux is plotted as a function of $(\rho_{LH} \times n_{e,launcher})$. $n_{e,launcher}$ is the density in front of the grill as defined in Figure 19.